



Research paper

SEAuAIS: A self-explainable autoencoder with AIS-based maritime anomaly detection

Harald Vilhelm Skat-Rørdam ^a, Rune D. Kjærsgaard ^a, Emil Hovad ^a,
Line K.H. Clemmensen ^{a,b,*}

^a Department of Applied Mathematics and Computer Science, Technical University of Denmark, Richard Petersens Plads, Building 324, Kgs. Lyngby, 2800, Denmark

^b Department of Mathematical Sciences, University of Copenhagen, Universitetsparken 5, Copenhagen, 2100, Denmark

ARTICLE INFO

Keywords:
Maritime safety
Anomaly detection
VAE
Explainable AI
Situational awareness
Physics-informed machine learning

ABSTRACT

Maritime anomaly detection systems aim to harness data from the automatic identification system (AIS) to enable early detection and prevention of imminent safety risks. Many existing systems are not interpretable and are also not evaluated in remote and sparsely traversed waters. This makes it challenging for operators to understand, adapt, and apply them effectively. This work aims to address both these gaps in the literature by introducing *SEAuAIS*: A novel, flexible anomaly detection framework based on the foundation of a self-explainable autoencoder model that incorporates physical constraints. We evaluate the model on two cases: anomalous vessel behavior following a cable breach in the remote waters around Svalbard and a search and rescue (SAR) emergency in a high-traffic zone near Bornholm Island. For both regions, we outperform state-of-the-art methods at significantly reduced compute time.

1. Introduction

The development of data-driven methods for the detection of maritime vessel anomalies represents an emerging field of research, especially utilizing the highly available Automatic Identification System (AIS) data. AIS data can be used to identify abnormal vessel behavior for maritime situational awareness and safety (Wolsing et al., 2022; Olesen et al., 2023a; Olesen, 2023).

In general, vessel monitoring is of great importance; ensuring human and environmental safety is a primary goal of vessel anomaly detection, preventing collisions like the one that occurred at Bornholm in December 2021 (Branch, 2023). Another critical aspect is the protection of undersea infrastructure which transmits 97 % of all internet traffic (NATO, 2019). There are an estimated 600 active submarine cables totaling 1.4 million kilometers (TeleGeography, 2025), along with several natural gas pipelines on the seabed. Breaks in these cables are costly and can have severe human and environmental consequences. Threats to these cables fall into three categories: natural, intentional, and unintentional human activity (NATO, 2019). Unintentional threats include activities such as fishing and anchoring. Multiple instances of cuts to critical infrastructure cables have been reported worldwide, such as near Taiwan (News, 2023), in the Red Sea (News, 2024; Ziady, 2024), and near Svalbard (Schia et al., 2023). Intentional activity has been considered but

not confirmed in these cases, partly due to frequent unintentional damage to maritime infrastructure. This emphasizes the high vulnerability of these cables, as recognized by NATO (2024), and underscores the need to detect abnormal activity near submarine cables.

Since AIS is mandatory (IMO, 2025) and provides real-time information about vessel positions, speeds, courses, and more, it has become a cornerstone of maritime tracking research. Guo et al. introduced an anomaly detection method using kinematic interpolation to identify irregularities in AIS trajectories (Guo et al., 2021). Their three-step approach—*data pre-processing*, *kinematic estimation*, and *error clustering*—effectively identifies abnormal AIS data points. Olesen et al. proposed a two-step clustering, using kinematic information for clustering, subsequent to a positional clustering, for anomaly detection (Olesen et al., 2023a). Nguyen et al. introduced *GeoTrackNet*, a neural network for detecting abnormal vessel behaviors in AIS data. It combines the strength of *probabilistic modeling* and *deep learning* to analyze vessel trajectories and flag anomalies, such as abrupt route deviations or unusual speed patterns (Nguyen et al., 2020). Building on this work, Nguyen and Fablet developed *TrAISformer*, a more advanced model for AIS-based vessel trajectory prediction (Nguyen and Fablet, 2024). *TrAISformer* employs a *probabilistic transformer architecture* and a *sparse, high-dimensional data representation* to handle the heterogeneous and multivariate nature of AIS data. By framing the prediction task as a classification problem,

* Corresponding author.

E-mail addresses: harsk@dtu.dk (H.V. Skat-Rørdam), rdokj@dtu.dk (R.D. Kjærsgaard), emilh@dtu.dk (E. Hovad), lkhc@dtu.dk; lkhc@math.ku.dk (L.K.H. Clemmensen).

the model accurately captures the multivariate nature of vessel trajectories. However, both architectures use a four-hot encoding of the AIS signals, making them restrictive to a pre-chosen region of interest. Maganaris et al. explored using *deep recurrent neural networks* (RNNs) for AIS data, presenting a framework to detect outliers in maritime environments (Maganaris et al., 2024). Their model, based on a bidirectional *Gated Recurrent Unit* (GRU) with recurrent dropouts, captures the temporal dynamics of AIS trajectories through an *encoder-decoder architecture*. By comparing observed motion patterns with reconstructed trajectories, the model identifies deviations using a thresholding mechanism. The study demonstrated the superior performance of deep recurrent models in capturing the complex and non-linear dynamics of vessel navigation.

To increase generalizability across regions of interest, we introduce a generative AI model for AIS trajectories, called *SEAuAIS*, which performs vessel anomaly detection and ship type classification. To demonstrate generalizability, we validate the model's performance in both high-traffic congested waters and open waters and demonstrate that transfer learning is possible between these regions. In addition, our method addresses the limitations of interpretability in previous modeling approaches by including self-explainability through vessel pantype modeling. Our approach is based on a modification of the self-explainable variational auto-encoder classifier *PanVAE* from Kjærsgaard et al. (2024). Our approach also incorporates physics-informed machine learning, a scientific machine learning (SciML) technique that embeds selected physical constraints relevant to sailing routes directly into the model architecture to improve accuracy and interpretability (Karniadakis et al., 2021; Cuomo et al., 2022). For AIS data processing, we adapt methods from Karageorgos (2024), Olesen et al. (2023b). We investigate the cable breach in January 2022 around Svalbard, Norway, and share our labeled dataset as open-source ([10.11583/DTU.28553462](https://doi.org/10.11583/DTU.28553462)). Furthermore, we evaluate *SEAuAIS* in the congested waters around Bornholm, where a maritime emergency occurred in December 2021 (Branch, 2023), and compare *SEAuAIS* performance to previously reported results for this search and rescue (SAR) event.

2. Data

2.1. AIS data processing

The AIS data are arranged in a matrix, \mathbf{x} , with 361 time points of four variables: longitude and latitude, which represent the vessel's east-west and north-south positions on Earth, respectively; speed over ground (SOG), which is the vessel's speed relative to the Earth's surface, measured in knots; and course over ground (COG), which is the vessel's direction of travel over the ground, measured in degrees. Each trajectory is 12 hours long and resampled by linear interpolation to a two-minute frequency to ensure uniform time intervals between data points. Trajectories shorter than 12 hours are zero-padded to maintain consistency, and trajectories shorter than 10 minutes are discarded due to a lack of data. Similarly, trajectories longer than 12 hours are split into smaller segments to maintain consistency, and if gaps exceed 45 minutes between consecutive transmissions for the same vessel, the trajectory is split; this accounts for potential discontinuities in the AIS data. Finally, the data are standardized based on the mean and standard deviation from the training data Appendix A.

SEAuAIS is a joint anomaly detection and classification model, therefore, we enrich the AIS data with vessel class information. Each AIS transmission includes a unique Maritime Mobile Service Identity (MMSI) number. The vessels are categorized into 5 classes (Commercial, Fishing, Passenger, Service, and Other), determined using this unique ID, as described in Appendix B. Our code is available here: [GitLab](https://gitlab.com/harsk/seauais-ocean-engineering)¹.

¹ <https://gitlab.com/harsk/seauais-ocean-engineering>

2.2. Anomalous cases and their train, validation, and test sets

We focus on the two geographic regions of interest (ROIs) shown in Fig. 1. Anomalies, or outliers, are patterns in data that do not conform to a well-defined notion of normal behavior (Chandola et al., 2009). In both cases, anomalous trajectories were identified by manually inspecting the AIS data for routes that deviated from typical vessel movement, such as exhibiting irregular patterns or remaining in locations where prolonged presence is atypical.

Svalbard case: We examine a ROI in the remote Arctic sea around the archipelago of Svalbard (Fig. 1(a)). In this region, we accessed AIS data from the Norwegian *Kystdatabaset* (2024). To our knowledge, this has not previously been analyzed in the literature. It poses a challenging scenario due to the sparse traffic in the region and the dramatic transformation of the Arctic seascape with the changing seasons as ice advances and retreats. We use all AIS data in the ROI for 2020 and 2021 as the training data. The test data spans the week around the submarine cable breach event (4–11 January, 2022). During this incident, one ship, MELKART-5, was notably associated with the event, as it sailed over the cable more than 30 times just before the connection was severed (Pomrenke, 2023; Flaaten et al., 2025, 2022). Furthermore, YAGRY was also in the vicinity and behaved similarly to MELKART-5. Based on the manual inspection process described above, we labeled 5 abnormal trajectories for YAGRY and 11 for MELKART-5, thus totaling 16 routes defined as anomalous. The labeled data can be found here: [10.11583/DTU.28553462](https://doi.org/10.11583/DTU.28553462).

Bornholm case: We analyze the ROI around the island of Bornholm in Danish waters (Fig. 1(b)), based on the SAR study from Olesen et al. (2023a) and the dataset published in Olesen et al. (2023b), which includes 25 anomalous routes labeled using the same manual inspection criteria. This region is characterized by high traffic and well-defined vessel lanes. The data consists of all AIS signals broadcast by vessels within the ROI from June to December 2021. We use June to December (except December 13) as training data and December 13, as test data, where MV SCOT CARRIER collided with KARIN HOEJ. This caused a maritime emergency, and nearby vessels were called to help with the SAR effort near the area of the incident to look for survivors. MV SCOT CARRIER initially continued its route after the collision and denied involvement (Branch, 2023).

Table 1 summarizes the data for the training, validation, test, and the two cases.

3. Method

3.1. Model architecture

The architecture of *SEAuAIS* is illustrated in Fig. 2 and is designed for the dual tasks of anomaly detection and vessel classification. It is built upon a variational autoencoder (VAE) framework, which learns a compressed latent representation of normal vessel trajectories. This architecture is augmented with a pantype mechanism. The pantypes are learnable representations that exist within the latent space and are dynamically updated during model training to represent archetypical route patterns.

3.1.1. Anomaly detection and classification criterion

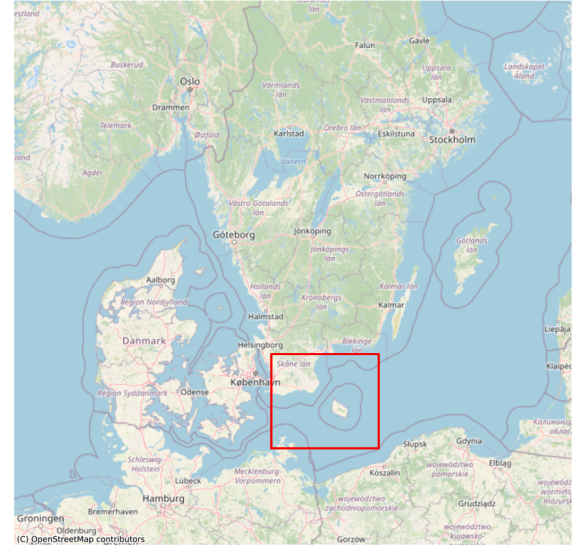
The model's architecture enables two distinct tasks:

Anomaly detection: The model's ability to reconstruct an input trajectory is used to detect anomalies. The reconstruction error, measured as the mean squared error (MSE) between the original trajectory \mathbf{x} and its reconstruction $\hat{\mathbf{x}}$, serves as the anomaly score. A trajectory is flagged as anomalous if this score exceeds a predefined threshold. This provides a statistical definition of an anomaly as a pattern that the model, trained on normal data, cannot effectively represent.

Vessel classification: In parallel, the model provides context by classifying vessels. The latent vector \mathbf{z} is compared to M pantypes



(a) ROI near the Svalbard archipelago, north of Norway (76.8°N, 7.9°E to 79.5°N, 17.2°E).



(b) ROI around Bornholm Island, south of Sweden (54.5°N, 13°E to 56°N, 16°E).

Fig. 1. ROIs in the study marked by the two squares: Svalbard to the left and Bornholm to the right. In the left plot, the twin submarine cables of interest are marked with dashed lines.

Table 1

Overview of the data used for training, validating, and testing the SEAuAIS in the Svalbard and Bornholm regions.

Svalbard	Value	Details
Train Data	2 years	Jan 2020 - Dec 2021
Test Data		
N. Days	8 days	Jan 4th - 11th, 2022
N. Anomaly Labels	16	Number of labeled trajectories
N. Anomalous Ships	2	MELKART-5 and YAGRY
ROI	(76.8°N, 7.9°E), (79.5°N, 17.2°E)	Bounding box coordinates
Train/Val Split	80/20	Random split: 80 % training, 20 % validation
Features (x)	4	Latitude, Longitude, SOG, COG
Length of a Trajectory	361	2-min sampling, 12-hour duration
Vessel Classes (y)	5	Commercial, Fishing, Other, Passenger, Service
Bornholm	Value	Details
Train Data	6 months	June 2021 - Dec 2021 (excl. Dec 13)
Test Data		
N. Days	1 day	Dec 13, 2021
N. Anomaly Labels	25	Number of labeled trajectories
N. Anomalous Ships	17	KARIN HOEJ, MV SCOT CARRIER, etc.
ROI	(54.5°N, 13°E), (56°N, 16°E)	Bounding box coordinates
Train/Val Split	80/20	Random split: 80 % training, 20 % validation
Features (x)	4	Latitude, Longitude, SOG, COG
Length of a Trajectory	361	2-min sampling, 12-hour duration
Vessel Classes (y)	5	Commercial, Fishing, Other, Passenger, Service

assigned to each vessel class, where M is fixed across all classes. This comparison yields a similarity score s , which is passed through a linear classifier h to produce the final vessel class prediction \hat{y} , thereby enforcing an interpretable structure on the latent space.

3.2. Model loss

SEAuAIS is trained by minimizing four loss terms:

$$\mathcal{L}_{\text{SEAuAIS}} = \mathcal{L}_{\text{pred}} + \mathcal{L}_{\text{VAE}} + \mathcal{L}_{\text{vol}} + \mathcal{L}_{\text{pan}}. \quad (1)$$

Each loss term is multiplied by a coefficient (see Table C.6), which controls its relative contribution to the total loss.

$\mathcal{L}_{\text{pred}}$ is the classification loss for the vessel type, given by:

$$\mathcal{L}_{\text{pred}} = \frac{1}{|\mathbf{X}|} \sum_{i=1}^{|\mathbf{X}|} \mathbf{CE}(h(s_i); y_i), \quad (2)$$

where \mathbf{CE} is the cross entropy with class labels y , \mathbf{X} is the set of trajectories and $|\mathbf{X}|$ the number of trajectories. The linear classifier h is based on similarities s_i between pantypes and vessel trajectories in latent space. The similarities s_i are defined as:

$$s_i(k, j) = \text{sim}(\mathbf{z}_i, \boldsymbol{\phi}_{kj}) = \log \left(\frac{\|\mathbf{z}_i - \boldsymbol{\phi}_{kj}\|^2 + 1}{\|\mathbf{z}_i - \boldsymbol{\phi}_{kj}\|^2 + \epsilon} \right), \quad (3)$$

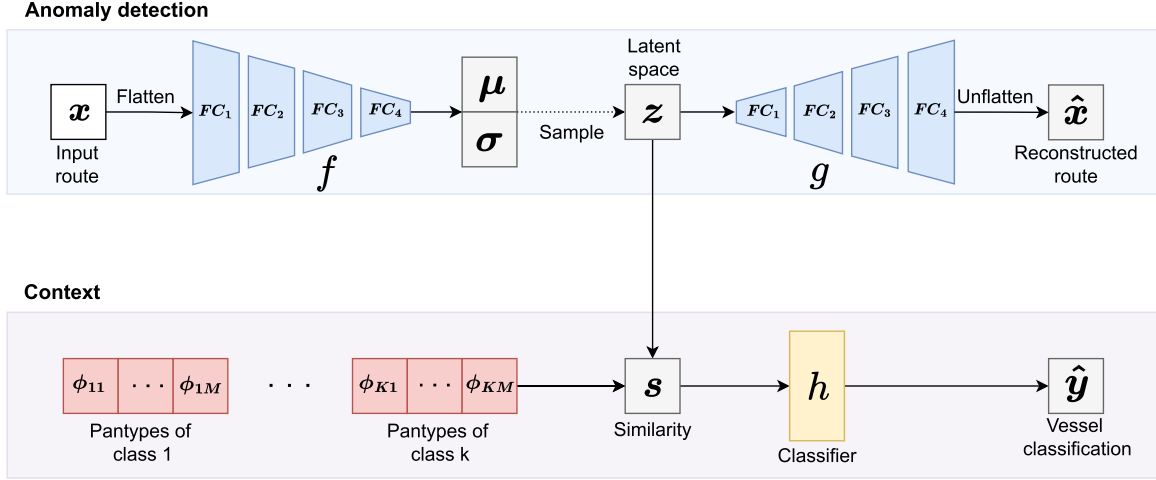


Fig. 2. Schematic of the SEAuAIS architecture. An n-dimensional tensor input trajectory x is passed through an encoder f to produce a latent distribution (μ, σ) , from which a vector z is sampled. The decoder g reconstructs the trajectory \hat{x} , while a parallel branch compares z to the set of learned latent pantypes ϕ_{kj} to classify the vessel type \hat{y} .

similarly to ProtoPNet in Chen et al. (2019). This gives us a similarity measure between the vessel trajectory i in the latent space, represented by z_i , and the j^{th} pantype within the k^{th} class, represented by ϕ_{kj} .

The classifier thus identifies distinct behaviors associated with each vessel class expressed through the similarity scores between the latent embeddings and the learned pantypes. Moreover, a comparison between actual ship class and predicted class can provide further context to anomalous behavior, as we demonstrate in Section 4.

\mathcal{L}_{VAE} represents the variational autoencoder (VAE) losses, which consist of two terms: 1) the reconstruction loss and 2) the KL-divergence (D_{KL}). The KL-divergence term accounts for a mixture of VAEs sharing the same network. This consists of one mixture per class and one component for each pantype. Each class VAE has a Gaussian prior distribution (\mathcal{N}) centered on each M class pantypes. Each mixture is trained using training data only from the corresponding class, and the mixture weights are then given by the similarities of all pantypes in the class (Gautam et al., 2022):

$$\begin{aligned} \mathcal{L}_{VAE} &= \frac{1}{|\mathbf{X}|} \sum_{i=1}^{|\mathbf{X}|} \left[\mathcal{L}_{recon_i} + \mathcal{L}_{KL_i} \right] \\ &= \frac{1}{|\mathbf{X}|} \sum_{i=1}^{|\mathbf{X}|} \left[\frac{1}{N_i \cdot N_F} \|x_i - \hat{x}_i\|^2 \right. \\ &\quad \left. + \sum_{k=1}^K \sum_{j=1}^M y_i(k) \frac{s_i(k, j)}{\sum_{l=1}^M s_i(k, l)} \right. \\ &\quad \left. \cdot D_{KL}(\mathcal{N}(\mu_i, \sigma_i) \| \mathcal{N}(\phi_{kj}, I_d)) \right], \end{aligned} \quad (4)$$

N_i is length of trajectory i , and N_F is the number of features (Table 1), $d \times d$ identity matrix (where d is the dimension of the latent space), K is the number of classes, and M is the number of pantypes per class.

\mathcal{L}_{vol} is a volumetric loss used to enhance pantype diversity. It is defined as:

$$\mathcal{L}_{vol} = \frac{1}{K} \sum_{k=1}^K \frac{1}{|\mathbf{G}_k|^{\frac{1}{2}}}, \quad (5)$$

where $\mathbf{G}_k \in \mathbb{R}^{M \times M}$ is the Gram matrix, computed as $\mathbf{G}_k = \Phi_k^T \Phi_k$. The pantype vectors ϕ_{kj} are the column vectors of the pantype matrix Φ_k . The determinant $|\mathbf{G}_k|$ (Gram determinant) quantifies the M -dimensional volume of the parallelotope formed by the pantype vectors in the d -dimensional latent space.

By minimizing this loss, the pantypes will diverge and occupy distinct regions of the latent space, effectively preventing pantype collapse. This approach enables pantypes to represent diverse aspects of the data distribution, further enhancing the ability of the model to capture a wide range of data variability.

3.2.1. Loss term for kinematic-based pantypes

\mathcal{L}_{pan} is a loss used to enhance the physical plausibility of the pantypes, and it consists of five loss terms to achieve this:

$$\mathcal{L}_{pan} = \mathcal{L}_{phys} + \mathcal{L}_{slow} + \mathcal{L}_{fast} + \mathcal{L}_{std} + \mathcal{L}_{land}. \quad (6)$$

\mathcal{L}_{phys} is a physics-based loss term that encourages physically plausible ship movement between consecutive positions.

$$\mathcal{L}_{phys} = \frac{1}{|\mathcal{K}| \cdot N_L \cdot M} \sum_{k \in \mathcal{K}} \sum_{j=1}^M \sum_{t=1}^{N_L-1} \left\| \hat{\mathbf{p}}_{k,j,t+1} - \mathbf{p}_{k,j,t+1} \right\|^2, \quad (7)$$

where \mathcal{K} is the set of classes k that exists in the data (y) for the specific ROI², N_L is the set length for the output of the decoder, M is the number of pantypes per class, $\mathbf{p}_{k,j,t}$ is the actual position (lat, lon) of the decoded (reconstructed) pantype j in class k at time t , and $\hat{\mathbf{p}}_{k,j,t+1}$ is the predicted next position, computed as:

$$\begin{aligned} \varphi_{t+1} &= \arcsin \left(\sin \varphi_t \cos \frac{d_t}{R} + \cos \varphi_t \sin \frac{d_t}{R} \cos \theta_t \right), \\ \lambda_{t+1} &= \lambda_t + \arctan2 \left(\sin \theta_t \sin \frac{d_t}{R} \cos \varphi_t, \cos \frac{d_t}{R} - \sin \varphi_t \sin \varphi_{t+1} \right), \end{aligned}$$

in which φ_t and λ_t are the current latitude and longitude (in radians), θ_t is the COG in radians, $d_t = v_{k,j,t} \cdot \Delta t$ is the distance traveled, $R = 6,371,000$ m is Earth's radius, Δt is the time interval, and $v_{k,j,t}$ is the speed over ground (in m/s) at time t for the decoded pantype j of class k .

\mathcal{L}_{slow} and \mathcal{L}_{fast} are used to ensure that the trajectory maintains speeds within realistic bounds, preventing movement that is either too slow or too fast.

$$\mathcal{L}_{slow} = \frac{1}{|\mathcal{K}| \cdot N_L \cdot M} \sum_{k \in \mathcal{K}} \sum_{j=1}^M \sum_{t=1}^{N_L-1} \max(0, v_{min} - v_{k,j,t})^2, \quad (8)$$

$$\mathcal{L}_{fast} = \frac{1}{|\mathcal{K}| \cdot N_L \cdot M} \sum_{k \in \mathcal{K}} \sum_{j=1}^M \sum_{t=1}^{N_L-1} \max(0, v_{k,j,t} - v_{max})^2, \quad (9)$$

² The total number of classes K is fixed at 5 (see Table 1), but not all classes are guaranteed to be represented in every region of interest.

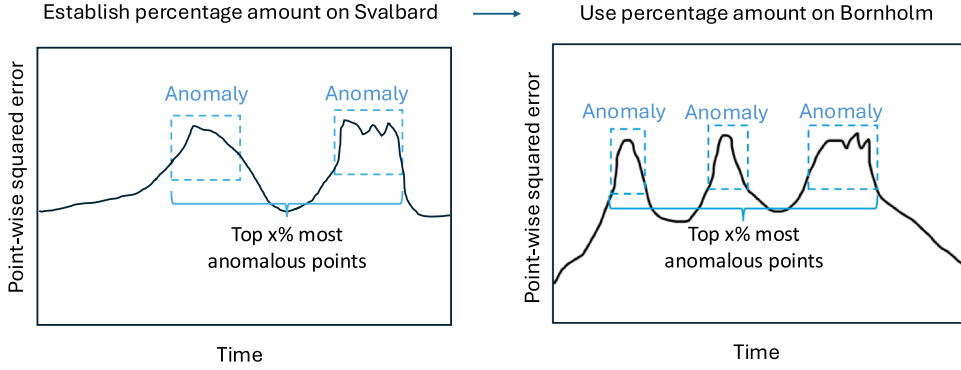


Fig. 3. Schematic representation of the mean squared error of the four features for each time point in a trajectory. The left figure shows the selection of the top $x\%$ most anomalous points on Svalbard, while the right figure validates this selection on Bornholm.

where $v_{\min} = 0.514444 \text{ m/s}$ is considered the slowest practical speed, and $v_{\max} = 10 \text{ m/s}$ is the maximal practical speed.³

\mathcal{L}_{std} encourages the spread (standard deviation) of locations in latitude and longitude to match the variability observed in the data for each class.

$$\mathcal{L}_{\text{std}} = \frac{1}{|\mathcal{K}|} \sum_{k \in \mathcal{K}} \left\| \begin{pmatrix} \sigma_k^{\text{lat}} \\ \sigma_k^{\text{lon}} \end{pmatrix} - \begin{pmatrix} \hat{\sigma}_k^{\text{lat}} \\ \hat{\sigma}_k^{\text{lon}} \end{pmatrix} \right\|^2, \quad (10)$$

where σ_k^{lat} and σ_k^{lon} are the standard deviations for each class k , defined as: $\sigma_k^{\text{lat}} = \sqrt{\frac{1}{N_k} \sum_{x_i \in \mathcal{X}_k} \|x_i^{\text{lat}} - \mu_k^{\text{lat}}\|^2}$, $\sigma_k^{\text{lon}} = \sqrt{\frac{1}{N_k} \sum_{x_i \in \mathcal{X}_k} \|x_i^{\text{lon}} - \mu_k^{\text{lon}}\|^2}$ in which $\mathcal{X}_k = \{x_i \in \mathbf{X} \mid y_i = k\}$, x_i is the i -th trajectory, y_i its label, $N_k = N_F \sum_{x_i \in \mathcal{X}_k} |x_i|$ is the total number of data points in class k , and the means are calculated as $\mu_k^{\text{lat}} = \frac{1}{N_k} \sum_{x_i \in \mathcal{X}_k} x_i^{\text{lat}}$, $\mu_k^{\text{lon}} = \frac{1}{N_k} \sum_{x_i \in \mathcal{X}_k} x_i^{\text{lon}}$, and $\hat{\sigma}_k^{\text{lat}}$ and $\hat{\sigma}_k^{\text{lon}}$ are the standard deviations for the decoded pantypes in class k , computed in the same way as for the trajectories in class k .

$\mathcal{L}_{\text{land}}$ encourages the predicted positions to remain over water and avoid land masses.

$$\mathcal{L}_{\text{land}} = \frac{1}{|\mathcal{K}| \cdot N_L \cdot M} \sum_{k \in \mathcal{K}} \sum_{j=1}^M \sum_{t=1}^{N_L} \text{BCE}(w(\mathbf{p}_{k,j,t}), 1), \quad (11)$$

with BCE denoting the binary cross-entropy loss, and $w(\mathbf{p}_{k,j,t})$ is the predicted water probability at position $\mathbf{p}_{k,j,t}$, computed by differentially sampling a Gaussian kernel-smoothed land/water map.

3.3. Route anomaly metric

Anomalies are identified by analyzing the route reconstruction loss, measured using the mean squared error (MSE). This is done by comparing the actual route (\mathbf{x}_i) to its predicted counterpart ($\hat{\mathbf{x}}_i$), calculated as $\text{MSE}_i = \frac{1}{N_i} \|\mathbf{x}_i - \hat{\mathbf{x}}_i\|^2$, where N_i is the length of \mathbf{x}_i . The input routes to SEAuAIS are up to 12 hours long, making anomalous behavior across the complete route unlikely. Additionally, analyzing the mean route behavior smooths out important local spatial and temporal behavior.

For this reason, we restrict the anomaly detection framework to points exhibiting highly anomalous behavior in short, localized temporal bursts, as shown in Fig. 3. To focus the attention of SEAuAIS on these localized anomalies, we define the anomaly score as the mean reconstruction loss of the top $x\%$ most anomalous points per route, ranked by point-wise squared error. This metric, $\text{MSE}_{x\%}$, is defined as:

$$\text{MSE}_{x\%,i} = \frac{1}{N_{i,x\%}} \sum_{n \in S_{i,x\%}} (\mathbf{x}_{i,n} - \hat{\mathbf{x}}_{i,n})^2, \quad (12)$$

³ These thresholds are chosen to exclude stationary or implausibly fast vessel movements. While vessels can achieve speeds outside this range, such cases are rare and/or not relevant for the pantype modeling.

where $N_{i,x\%} = \min(N_i, x\% \cdot N_{SL})$ is the number of selected anomalous points, where N_{SL} represents the fixed sequence length to which all trajectories are zero-padded, and $S_{i,x\%}$ is the set of the $N_{i,x\%}$ points with highest reconstruction errors for trajectory i . To evaluate the impact of x , we analyze three different values: 5% (18 points), 10% (36 points), and 20% (72 points).

3.4. Performance metrics

We use three sets of performance metrics to evaluate our model. The first set of metrics includes the area under the curve (AUC) and optimal threshold values (τ), both derived from the receiver operating characteristics (ROC). We calculate AUC scores across different percentages of the most anomalous points (as described in Section 3.3) to determine the optimal percentage to use while also comparing against using all trajectory points. For each approach (optimal percentage and all points) and each ROI, we determine an optimal threshold τ on the ROC curve by maximizing the difference between the True Positive Rate (TPR) and False Positive Rate (FPR): $\tau^* = \arg \max_{\tau} (\text{TPR}(\tau) - \text{FPR}(\tau))$. We then evaluate model performance at these optimal threshold points.

The second set of metrics consists of recall, precision, and F1 score, which evaluate the model's ability to identify anomalous trajectories correctly. We report these metrics for the two regions, using the optimal thresholds established from the ROC curves.

The third set of metrics is computational efficiency, which is assessed through two measurements: the training time to convergence on a GPU and the time required to process a trajectory at inference on a GPU. Detailed specifications for both systems are provided in Appendix C.

3.5. Model training and experiments

For both Svalbard and Bornholm, SEAuAIS is trained separately on each region's complete AIS training set. The results from the trained networks consist of vessel anomaly identification and explainability provided by pantypes and vessel type classifications.

To evaluate the model's performance, we first consider the Single Region scenario where SEAuAIS is trained and tested on the same ROI, either Svalbard or Bornholm.

Due to the limited availability of labeled datasets, most research in maritime anomaly detection does not examine cross-region model performance. This is a significant limitation, as the concepts learned by models may be highly region specific, and retraining models for each new region is both time- and resource-intensive. To address this, we evaluate the generalizability of the SEAuAIS model by conducting experiments on two distinct maritime regions: Svalbard and Bornholm, and conducting transfer learning experiments between the two. These regions differ in navigational behavior, vessel types, environmental conditions, and particularly in their anomaly event types, making

Table 2

AUC scores for anomaly detection using different $MSE_{x\%}$ for Svalbard and Bornholm. Optimal AUC is **bolded**.

$MSE_{x\%}$	$MSE_{5\%}$	$MSE_{10\%}$	$MSE_{20\%}$	$MSE_{100\%}$
AUC Score (Svalbard)	0.84	0.82	0.80	0.68
AUC Score (Bornholm)	0.93	0.93	0.93	0.92

Table 3

Bornholm and Svalbard incident AUC scores and inference times for the different models, with optimal results **bolded** for each ROI.

Model	AUC		Inf. Time (ms)
	Bornholm	Svalbard	
VRNN	0.91	0.74	4.35
RVAE	0.91	0.71	0.76
TrAISformer	0.91	0.81	64.09
SEAuAIS	0.93	0.84	0.012

them ideal for assessing the model's adaptability. The ability to generalize well across different locations is essential to ensure reliable anomaly detection and classification without the need for extensive retraining.

In these experiments, we conduct two types of generalizability tests, each performed both with and without the kinematic loss for the pantypes, \mathcal{L}_{pan} , and compare the results to the **Single Region** baseline. The two tests are: **1. Direct Transfer**: SEAuAIS is trained on one ROI (e.g., Svalbard) and evaluated directly on another ROI (e.g., Bornholm) without further training. **2. Fine-Tuning**: SEAuAIS is first trained on one ROI, then fine-tuned on the training set of a second ROI, and finally evaluated on the test set of that region. For each test, we consider two training strategies: **A**. Models initially trained without \mathcal{L}_{pan} , where \mathcal{L}_{pan} is only introduced during fine-tuning, and **B**. Models trained with \mathcal{L}_{pan} throughout all training phases. In total, this results in five experimental setups, including the baseline. This distinction is necessary because \mathcal{L}_{pan} is region-specific: the loss terms \mathcal{L}_{land} and \mathcal{L}_{std} are automatically computed using statistics and land/water maps unique to each region of interest (ROI).

3.5.1. Ablation study

To quantify the contribution of each loss component, we perform an ablation study on the Svalbard region. In each experiment, a single loss term is removed, and the model is retrained and evaluated from scratch. We report the resulting AUC for anomaly detection, providing

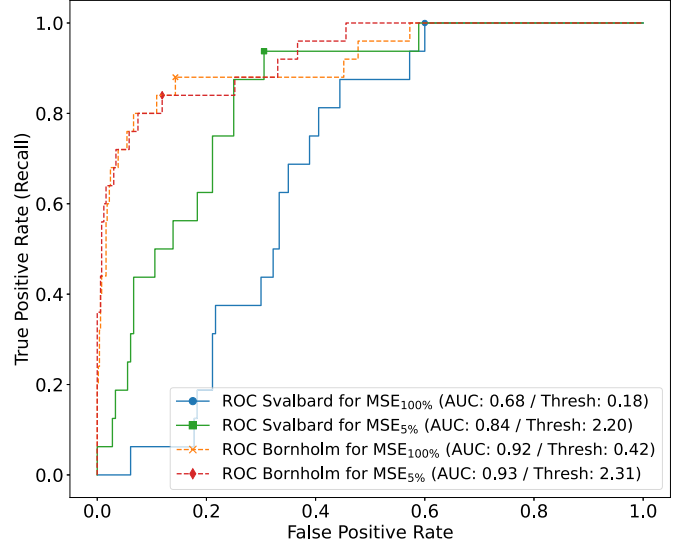


Fig. 4. The ROC curves with optimal reconstruction error thresholds τ for Svalbard and Bornholm, both with $MSE_{100\%}$ (using all points) and the $MSE_{5\%}$ approach.

a direct measure of each component's impact on overall performance. For qualitative comparison, we compare representative pantype trajectories between the baseline model and each ablation variant. In addition, we include UMAP projections of the learned latent space across models.

4. Results and discussion

We first present the results of SEAuAIS for each ROI separately, then compare these to its generalizability for the three scenarios across ROIs. Last, we examine the explainability provided by SEAuAIS. The loss curves and the model parameters are provided in [Appendix C](#).

4.1. Single region performance

Using the top 5 % most anomalous points in a trajectory to calculate the MSE ($MSE_{5\%}$) provides optimal performance with an AUC of 0.84 on the Svalbard data, as shown in [Table 2](#). While fewer points might further improve AUC, we consider 5 % the lower limit to ensure adequate data

Table 4

Performance metrics across generalizability scenarios. **AUC** is the primary evaluation metric. Optimal results are **bolded** for Svalbard and Bornholm, respectively. Training time in minutes is shown where applicable. For fine-tuning, the initial training time is not included in the total time.

Single Region						
ROI	AUC	Recall	Precision	F1	mins	
Svalbard	0.84	0.94	0.21	0.35	128	
Bornholm	0.93	0.84	0.26	0.40	394	
A. Without \mathcal{L}_{pan}						
1. Direct Transfer			2. Fine-tuning			
ROI	AUC	Recall	Precision	F1	mins	
Svalbard	0.81	1.00	0.17	0.29	-	
Bornholm	0.87	0.88	0.17	0.29	-	
B. With \mathcal{L}_{pan}						
1. Direct Transfer			2. Fine-tuning			
ROI	AUC	Recall	Precision	F1	mins	
Svalbard	0.84	1.00	0.22	0.36	-	
Bornholm	0.87	0.88	0.20	0.32	-	

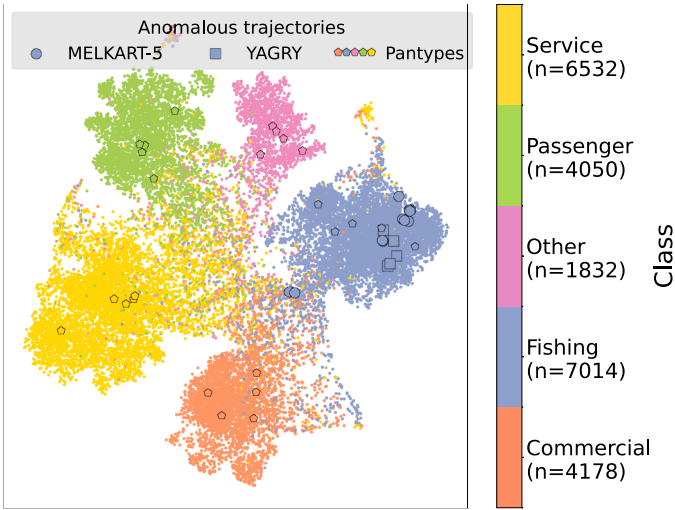


Fig. 5. UMAP for the Svalbard case of the latent space variable z . Square markers represent all anomalous MELKART-5 and YAGRY trajectories in the test data, colored by their true vessel type, and pentagonal markers indicate pantypes.

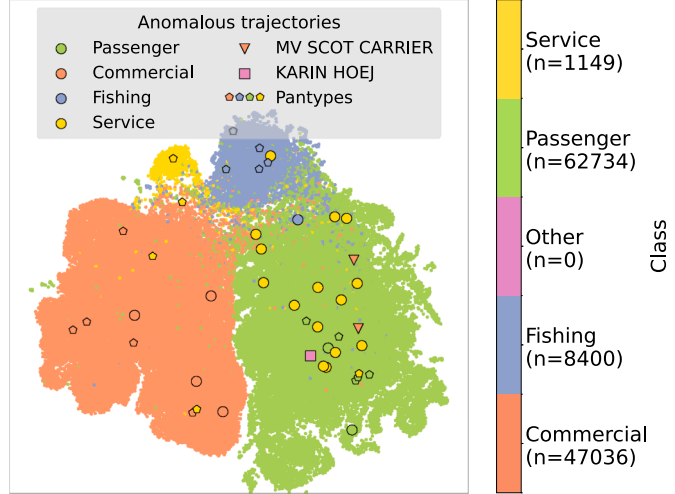


Fig. 6. UMAP of the latent space variable z for Bornholm. Circle markers represent all anomalous trajectories in the test data, colored by their true vessel type, with MV SCOT CARRIER and KARIN HOEJ having distinct markers. Pentagonal markers indicate pantypes.

for reliable detection without being excessively influenced by outliers. The results demonstrate that focusing on the most anomalous points significantly outperforms using all trajectory points ($MSE_{100\%}$), which achieves an AUC of 0.68. This difference is further illustrated in Appendix D with a visualization of the reconstruction errors for Svalbard. Note that for Bornholm, no significant difference in AUC is observed between the usage of different $MSE_x\%$ values.

The ROC curves and optimal thresholds τ for Svalbard and Bornholm are illustrated in Fig. 4. SEAuAIS achieves an AUC of 0.92 on Bornholm when using all points ($MSE_{100\%}$), which increases to 0.93 with the $MSE_5\%$ approach. For Svalbard, the AUC improves from 0.68 ($MSE_{100\%}$) to 0.84 ($MSE_5\%$). The optimal anomaly detection thresholds for the $MSE_5\%$ method are 2.20 for Svalbard and 2.31 for Bornholm.

The results for the two regions individually (Single Region) in Table 4 show significantly higher recall than precision for both regions. For Svalbard, SEAuAIS correctly predicts 15 out of 16 anomalous trajectories, with a recall of 94% and a precision of 21% giving an F1 score of 0.35. For Bornholm, SEAuAIS correctly predicts 21 out of 25

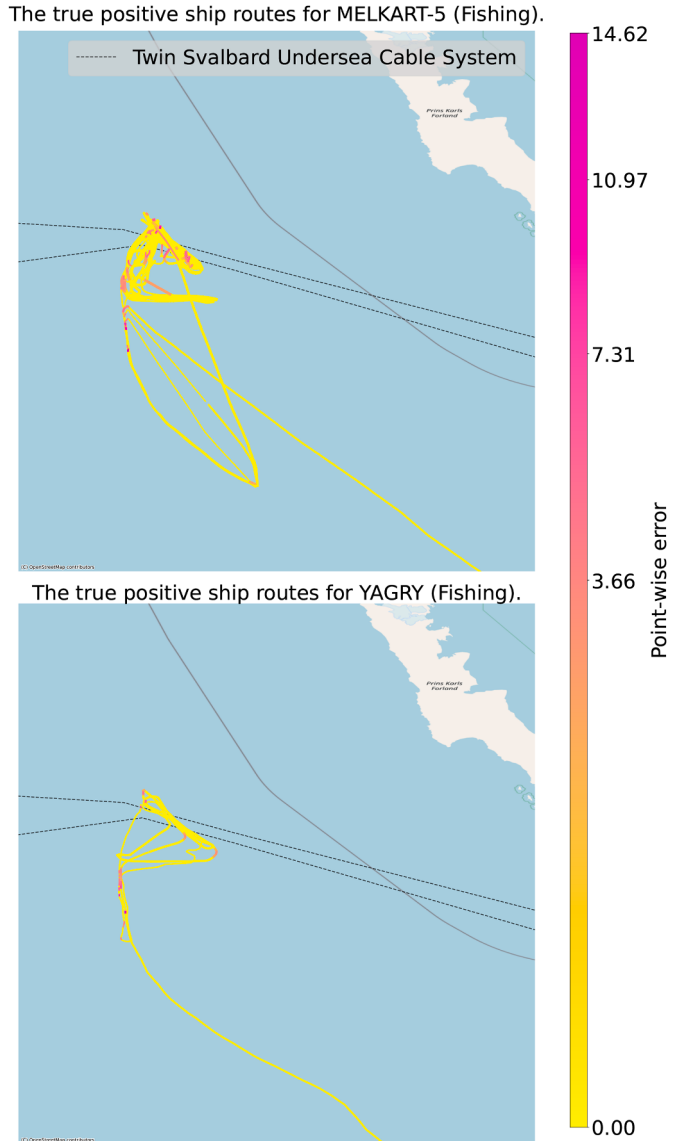


Fig. 7. The top figure shows the 10 true positive MELKART-5 routes, and the bottom figure shows the 5 true positive YAGRY routes. The routes are colored by point-wise error, with the values indicated by the color bar, as defined in the Code.

anomalous trajectories, achieving a recall of 84% and a precision of 26%, resulting in an F1 score of 0.40. The low F1 scores for both Svalbard and Bornholm highlight the balance between detecting anomalies (TPR) and avoiding an overwhelming FPR.

Several approaches could improve precision without negatively affecting the model's recall performance, thus improving the F1 score. This can be achieved through methods like port filtering. Vessels in ports can generate AIS signals, and these stationary signals deviate from normal movement patterns, causing the model to flag them as anomalous, thus causing a higher FDR. Additional context features could further enhance anomaly detection capabilities. Vessel-specific attributes such as type, size, and draft could enable more accurate reconstructions by accounting for inherent maneuverability differences between vessel classes. Integrating spatial context, such as proximity to critical infrastructure, regulatory boundaries, restricted zones, and established shipping lanes, could provide valuable discriminatory features. We expect such enhancements to reduce the FDR substantially while maintaining the model's recall (TPR) performance.

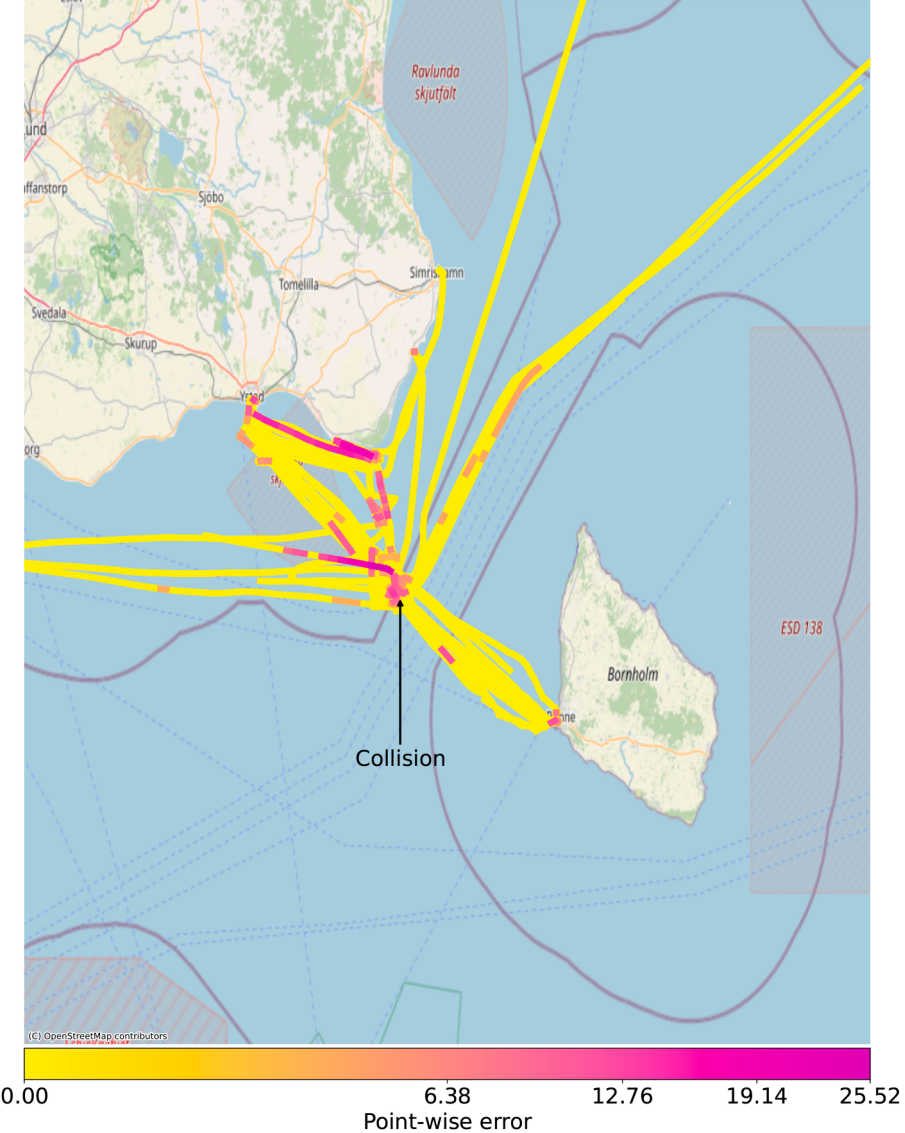


Fig. 8. All routes classified as anomalous by SEAuAIS. The routes are colored by the point-wise error, with the values indicated by the color bar, as defined in the Code.

4.2. Comparison to baseline models

We compare SEAuAIS to state-of-the-art models: VRNN (GeoTrackNet) (Nguyen et al., 2021), RVAE (Murray and Perera, 2021), and TrAISformer (Nguyen and Fablet, 2021), using the same detection criteria (Table 3). SEAuAIS achieves the highest AUC for both regions, exceeding TrAISformer by 0.02 on Bornholm and 0.03 on Svalbard, and is dramatically faster at inference ($5340\times$ faster than TrAISformer, $63\times$ faster than RVAE). Training times are also significantly reduced (see Appendix F for a full comparison of baseline model metrics and hyperparameters).

4.3. Ablation study

As summarized in Table S1, the AUC for anomaly detection remains largely unchanged across most ablation models, except for the reconstruction loss ($\mathcal{L}_{\text{recon}}$), where performance drops substantially, and the volumetric loss (\mathcal{L}_{vol}), where a slight increase is observed.

Qualitative effects of ablating individual loss terms are shown in Supplementary Figures S2-S8. Removing the classification loss $\mathcal{L}_{\text{pred}}$ leads to poor class separation in the latent space, with pantypes clustering incorrectly. Removing the KL-divergence term \mathcal{L}_{KL} also results in pantype

grouping, though class separation is partially preserved. Excluding the volumetric loss \mathcal{L}_{vol} causes pantype collapse, with multiple pantypes occupying the same region of latent space. Omitting the physics-based loss $\mathcal{L}_{\text{phys}}$ produces unrealistic, erratic pantype trajectories.

Further, removing the speed constraints $\mathcal{L}_{\text{fast}}$ and $\mathcal{L}_{\text{slow}}$ allows pantypes to attain implausible speeds, including negative values. Without the spread regularization \mathcal{L}_{std} , pantypes become overly concentrated and less informative. Excluding the land avoidance term $\mathcal{L}_{\text{land}}$ results in pantypes traversing land areas, and ablating the full kinematic loss \mathcal{L}_{pan} further degrades the physical plausibility of pantype trajectories.

Overall, while quantitative anomaly detection performance is robust to most ablations, the qualitative structure and interpretability of the learned pantypes are strongly dependent on the inclusion of each loss component.

4.4. Generalizability across regions

The results of the generalization tests are summarized in Table 4. For both Svalbard and Bornholm, fine-tuning leads to marginal improvements, and overall performance is similar whether the model is trained directly on the target region or fine-tuned from another region. The

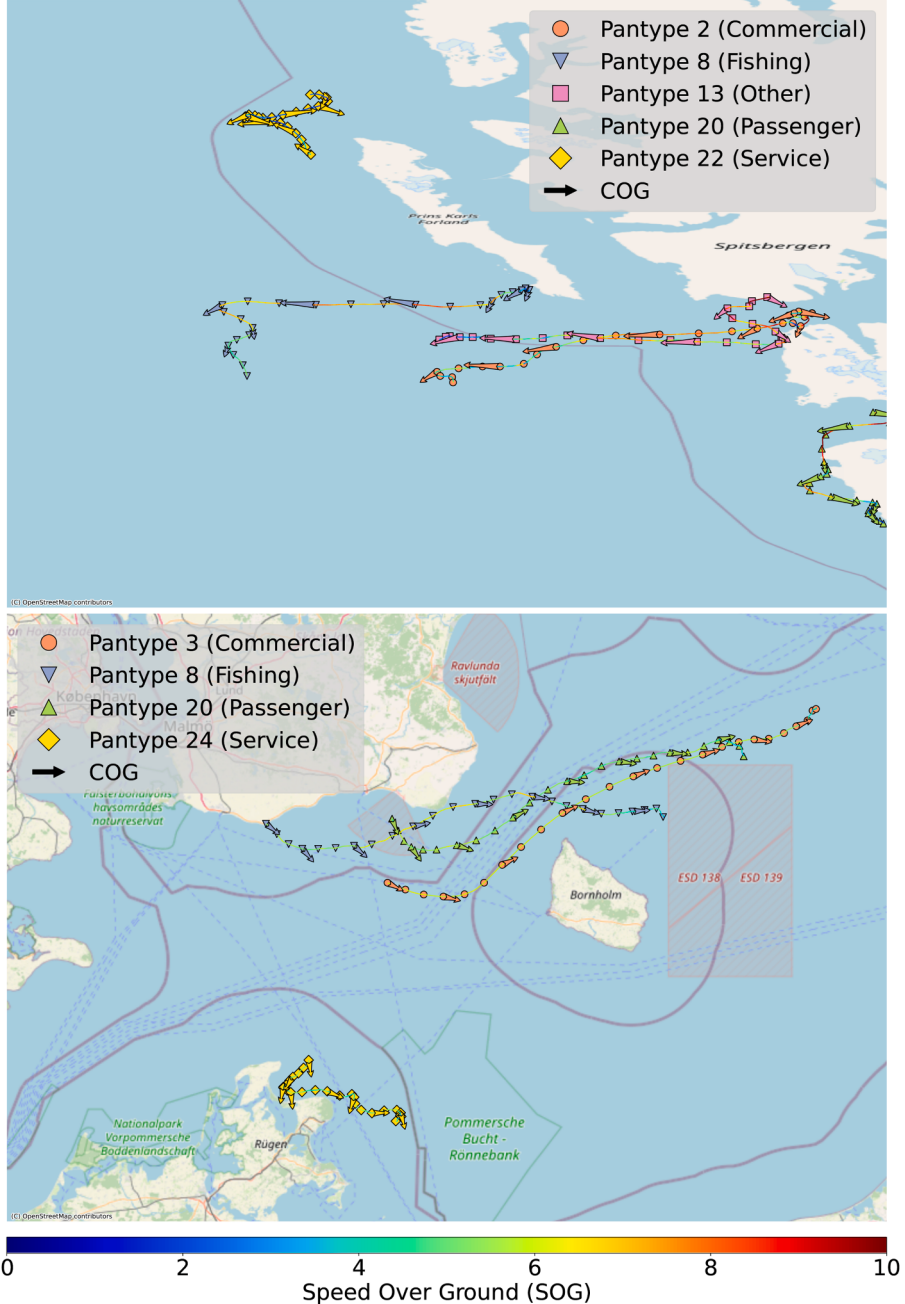


Fig. 9. One selected pantype for each class from Svalbard and Bornholm. For Bornholm, no “Other” class data exists in the training set, so the corresponding pantype is excluded. Lines represent the speed over ground (SOG), with values indicated by the color bar at the bottom, while arrows indicate the course over ground (COG).

model’s simple linear architecture likely contributes to its adaptability and ability to generalize across regions. Nevertheless, although L_{pan} incorporates the region-specific loss terms L_{land} and L_{std} , we do not observe any significant impact on the model’s regional specificity or its capacity to transfer between regions.

When SEAuAIS is applied directly to the Bornholm region without additional training, it achieves performance comparable to existing state-of-the-art methods Table 3. Notably, further fine-tuning on Bornholm data yields results that outperform these methods. This indicates that SEAuAIS possesses strong generalizability. These findings suggest that SEAuAIS primarily captures general behavioral patterns, such as SOG, COG, and abrupt trajectories, rather than relying on local routes or seasonal effects.

Focusing on the training times in Table 4 (mins), Svalbard exhibits a substantial reduction in training time, approximately 50 % when fine-tuning rather than training from scratch. For Bornholm, the reduction is less pronounced, with a 27 % decrease in case A and only 7 % in case B. These differences between regions are likely due to the larger training set size for Bornholm compared to Svalbard. We expect that pre-training SEAuAIS on larger datasets would result in further reduced training time improvements as well as improved results when using direct transfer.

This generalizability is attributable to the model architecture. Unlike VRNN and TrAISformer, which depend on region-specific binning and high-dimensional discrete inputs (Table F.8), SEAuAIS utilizes raw, continuous AIS features. This design enables the latent space to capture general vessel dynamics, while pantypes represent region-specific pat-

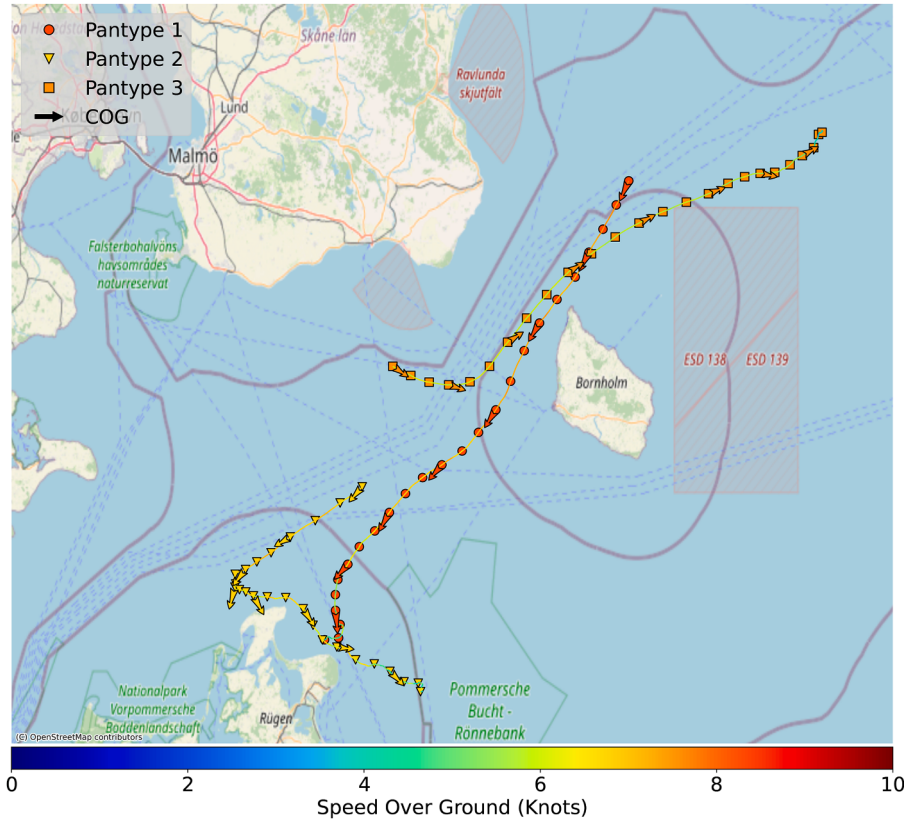


Fig. 10. Three selected pantypes from the Commercial class for the Bornholm region. Lines represent the SOG, with values indicated by the color bar at the bottom, while arrows indicate the COG.

terns. Consequently, SEAuAIS can be pre-trained on diverse data and adapted to new regions without fine-tuning. If further optimization or enhanced region-specific explainability is required, the model and/or pantypes can be fine-tuned as needed.

While SEAuAIS demonstrates strong generalization performance, regional differences, such as the fundamentally different error distributions observed between Svalbard and Bornholm, can impact transferability. For example, Svalbard exhibits a more uniform error distribution across trajectories, whereas Bornholm shows a highly right-skewed, power-law-like distribution (see Appendix E, Fig. E.14). This makes establishing a common anomaly threshold across regions challenging, as threshold selection affects each region differently.

4.5. Model validation and explainability

The learned latent spaces of the training data are visualized as two-dimensional UMAP projections (McInnes et al., 2018) for Svalbard and Bornholm in Figs. 5 and 6. The latent spaces (z) show reasonably well-separated classes, although some overlap occurs. This overlap may result from vessels behaving differently than expected for their class, from dual-purpose vessels that change their operational patterns seasonally, or because some classes have fewer observations and/or higher variance in vessel behavior.

Examining the Svalbard case (Fig. 5), all pantypes are placed within the mass centers for their vessel type. MELKART-5 and YAGRY are correctly identified as fishing vessels for all routes in the test data. This is not surprising, as these trajectories display the typical trawling patterns similar to the behavior of other fishing vessels. However, the anomaly detection values shown in Fig. 7 suggest that such fishing behavior directly over submarine cables is uncommon in this region. Notably, based

on AIS timestamps, we confirm that both ships sailed over the cables simultaneously.

The Bornholm case (Fig. 6) has a significant imbalance in class sizes, along with a complete absence of the “Other” class in the training data. The heterogeneous nature of the service class, including Military, Pilot Boats, and Research Vessels, makes the pantypes for this class more diverse than for the other classes. Many vessels with anomalous trajectories exhibit behavior similar to passenger ships, as most anomalous trajectories are placed in the Passenger class, including MV SCOT CARRIER and KARIN HOEJ. However, only two of these trajectories belong to passenger ships, likely due to the nature of the Bornholm incident. This incident caused a behavioral shift in the surrounding vessels, with more sporadic trajectories, particularly prevalent in the Passenger class. This is likely the reason we observe a significantly lower test accuracy compared to validation and training accuracies (see Appendix C, Fig. C.12(a)). To further illustrate these findings, Fig. 8 shows the behavior, according to SEAuAIS, of all vessels detected as anomalous in the area.

It is clear that most anomalous behavior occurs near the incident or involves vessels sailing directly to the incident.

To illustrate the self-explainability of the model, we have plotted a pantype for each class for both Svalbard and Bornholm in Fig. 9.

Examining the inter-class dynamics for Svalbard (top figure), we observe distinct behaviors for each class. The commercial pantype shows a trajectory originating from the main port in Svalbard (Port Longyear). The fishing pantype displays the characteristic zigzag pattern typical of trawling or fishing activity at the end of the trajectory. The passenger pantype follows a route suggestive of a sightseeing tour, sailing near the coast before heading away. The “Other” and service pantypes exhibit more sporadic and less defined trajectories, which is representative of the ships in these categories.

For the Bornholm region (bottom figure), similar patterns are observed. Notably, the shipping lanes between Bornholm and Sweden are heavily trafficked, as all pantypes in this region utilize these routes, but with different directions, destinations, and origins.

Finally, looking at the intra-class dynamics for the commercial class in the Bornholm region in Fig. 10. Here we see three distinct commercial routes: one (orange) coming from Zealand and heading north of Bornholm, another (red-orange) coming from the North of Bornholm heading south, and finally one (yellow-orange) sailing near the coast and presumably heading toward Świnoujście.

Although we use a fixed number of pantypes per class (M) in our experiments, the model architecture inherently supports a variable number of pantypes per class. However, it does not currently support learning the appropriate number during training. This could be addressed using simple heuristics such as those proposed in Kjærsgaard et al. (2024), where pantypes can be eliminated when deemed unnecessary by the model by inspecting the number of input trajectories they represent. More advanced methods could involve architectural modifications to enable adaptive pantype selection. We leave this as a direction for future research.

While the core architecture of SEAuAIS is based on a standard fully connected VAE, the primary novelty of our framework lies in the introduction of pantypes as a conceptually grounded representation of maritime behavior that enhances interpretability and supports more transparent anomaly detection. This behavioral abstraction allows operators to better understand and trust the model's decisions, as anomalies are linked to deviations from familiar and meaningful patterns rather than abstract latent vectors. Additionally, the incorporation of physics-based losses ensures that reconstructions and latent representations respect domain-specific constraints, further improving model reliability. We deliberately chose a simple architecture to focus attention on these core contributions and to demonstrate that significant performance gains can be achieved through informed design rather than architectural complexity. This choice also yields practical benefits. The model achieves an over 5000-fold speed-up in inference time compared to existing high AUC methods like the transformer-based TrAISformer, while still outperforming them in detection accuracy. We believe this combination of interpretability, efficiency, and effectiveness marks a meaningful advancement in maritime anomaly detection.

5. Conclusion

SEAuAIS outperforms state-of-the-art algorithms for anomaly detection in the Bornholm region for a SAR incident and identifies operator-confirmed anomalous trajectories in the Svalbard region. It also provides contextual awareness through the classification and archetypical modeling of vessel behavior using pantypes. To our knowledge, the Svalbard case has not been studied in the literature, and this marks the first time a cable breach anomaly has been automatically detected with AIS data, providing a basis for future comparisons with an AUC of 0.84 on our published data. SEAuAIS achieves a 94% recall rate, identifying all but one labeled anomalous trajectory. Comparing our Bornholm results to other state-of-the-art models, SEAuAIS achieves a superior AUC of 0.93 (versus 0.91 achieved by TrAISformer) while being 5340x faster at inference. Despite these improvements, the Svalbard and Bornholm models still suffer from low precision, resulting in low F1 scores. Therefore, we recommend that future research focus on improving precision while maintaining high recall and computational efficiency.

In our transfer learning experiments, we demonstrated the generalizability and robustness of SEAuAIS, which showed robust performance

across different training scenarios and even performed well without fine-tuning for the specific regions of interest.

Beyond performance metrics and generalizability, SEAuAIS offers self-explainable insights through interpretable pantypes and vessel classification capabilities. This classification capability enables the system to distinguish between different types of anomalies: Vessels exhibiting typical class behavior in atypical locations (Svalbard case) versus vessels displaying atypical class behavior (Bornholm case).

CRediT authorship contribution statement

Harald Vilhelm Skat-Rørdam: Writing – review & editing, Writing – original draft, Visualization, Validation, Software, Methodology, Investigation, Formal analysis, Data curation; **Rune D. Kjærsgaard:** Writing – review & editing, Writing – original draft, Visualization, Validation, Software, Methodology, Investigation, Formal analysis, Data curation, Conceptualization; **Emil Hovad:** Writing – review & editing, Writing – original draft, Visualization, Validation, Software, Methodology, Investigation, Formal analysis, Data curation; **Line K.H. Clemmensen:** Writing – review & editing, Supervision, Resources, Project administration, Methodology, Investigation, Funding acquisition, Conceptualization.

Data availability

Data created for this study is freely available at DOI: [10.11583/DTU.28553462](https://doi.org/10.11583/DTU.28553462).

Declaration of competing interest

The authors declare the following financial interests/personal relationships which may be considered as potential competing interests: Line K. H. Clemmensen reports financial support was provided by the Danish Defence. If there are other authors, they declare that they have no known competing financial interests or personal relationships that could have appeared to influence the work reported in this paper.

Acknowledgements

Funding: This work was partially funded by the Danish Defense.

Supplementary material

Supplementary material associated with this article can be found, in the online version, at [10.1016/j.oceaneng.2025.122656](https://doi.org/10.1016/j.oceaneng.2025.122656)

Appendix A. Reproducibility

The two datasets used in our case studies are available online: the Svalbard dataset via DOI: [10.11583/DTU.28553462](https://doi.org/10.11583/DTU.28553462)⁴ and the Bornholm dataset from (Olesen et al., 2023b). All code used in this project can be accessed through our [GitLab repository](#)⁵.

Appendix B. Vessel classification

We connect the vessel MMSIs to their associated vessel classes. To simplify the dataset, we reduce the number of classes by grouping smaller vessel categories into five general classes as described in Table B.5.

⁴ <https://doi.org/10.11583/DTU.28553462>

⁵ <https://lab.compute.dtu.dk/harsk/seauais-ocean-engineering>

Table B.5

Vessel type categories.

Category	Description
Commercial	Includes Tankers, Cargo Ships, and Supply Ships.
Fishing	Comprises all types of Fishing Vessels.
Passenger	Includes Passenger Ships, High-Speed Crafts (HSC), Pleasure Crafts, Sailing Vessels, and Yachts.
Service	Covers a range of vessels, including Research Vessels, Patrol Vessels, Military Operations Ships, Pilot Boats, Port Tenders, Ice Breakers, Lighthouse Vessels, Pollution Control Vessels, and Offshore Support Vessels.
Other	Includes vessels that do not fit into the categories above, such as those classified as Resolution 18 ships and other unspecified types.

Appendix C. Training details

The model parameters for SEAuAIS are listed in [Table C.6](#). We use the same number of prototypes and loss coefficients as the original Pan-VAE ([Kjærsgaard et al., 2024](#)). Early stopping is applied based on the validation set. SEAuAIS is trained on an RTX A5000 GPU with 24GB VRAM, an EPYC 9124 16c/32t @ 3.0 GHz CPU, utilizing 8 threads and 128 GB of memory.⁶

Table C.6

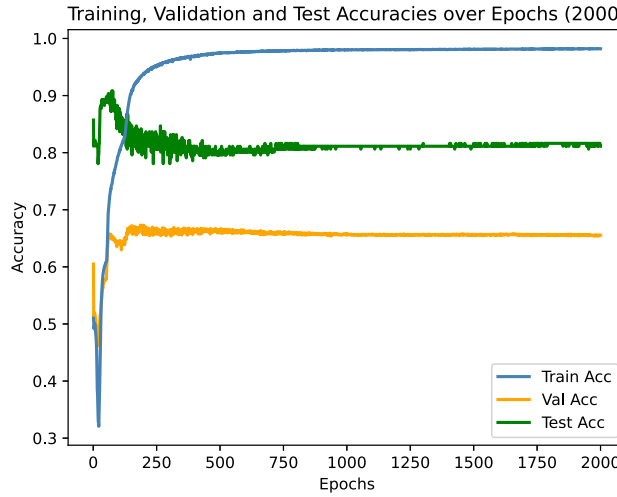
Overview of the model's parameters. The loss coefficients are $[\mathcal{L}_{\text{pred}}, \mathcal{L}_{\text{recon}}, \mathcal{L}_{\text{kl}}, \mathcal{L}_{\text{vol}}]$ and for \mathcal{L}_{pan} : $[\mathcal{L}_{\text{phys}}, \mathcal{L}_{\text{slow}}, \mathcal{L}_{\text{fast}}, \mathcal{L}_{\text{std}}, \mathcal{L}_{\text{land}}]$.

Parameter	Value
Data shape	(N, sequence length, features)
Features	4
Sequence length	361
N [train, test] (Svalbard)	[23,435 196]
N [train, test] (Bornholm)	[119,319 521]
Data normalization	Standardization
Padding and masking	Yes
Batch size	64
z dimension	128
Epochs	2000
Early stopping	200 ^a
Prototypes per class	5
Loss coeffs	[1, 1, 0.1, 1]
\mathcal{L}_{pan} coeffs	[10, 1, 1, 1, 0.1]
Learning rate	1e-4
N _{encoder} layers	4
N _{decoder} layers	4
Layer type	Fully connected (FC)
Optimizer	Adam optimizer

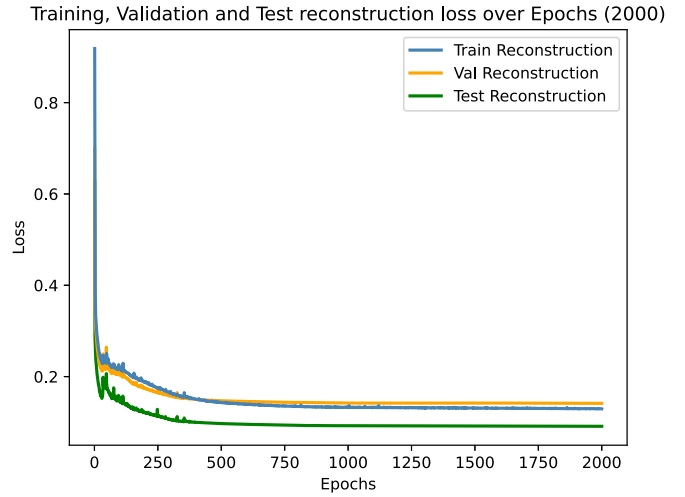
^a 100 for fine-tuning.

[Figs. C.11](#) and [C.12](#) illustrates the training, validation, and test accuracy and reconstruction curves for Svalbard and Bornholm respectively.

⁶ Due to the relatively simple architecture of SEAuAIS, training times do not vary significantly across different system specifications, including CPU-based setups.

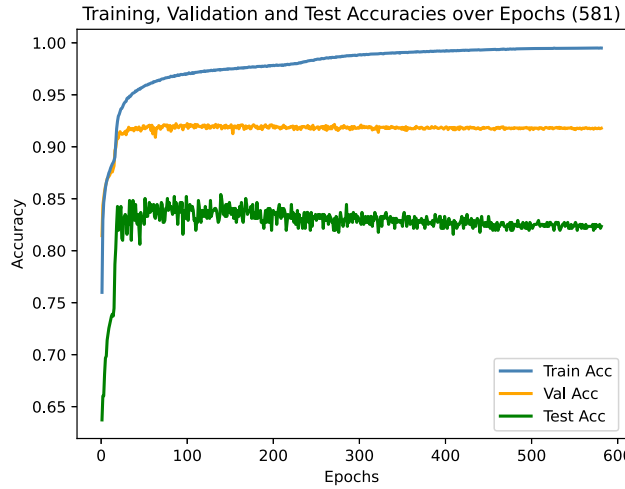


(a) Train, validation, and test accuracies for Svalbard.

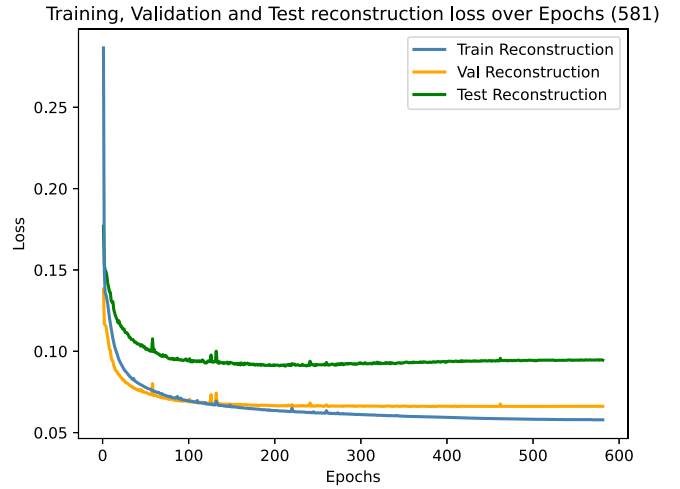


(b) Train, validation, and test reconstruction losses for Svalbard.

Fig. C.11. Training performance for the Svalbard area.



(a) Train, validation, and test accuracies for Bornholm.



(b) Train, validation, and test reconstruction losses for Bornholm.

Fig. C.12. Training performance for the Bornholm area.

Appendix D. Anomaly metric

Fig. D.13 shows a histogram of the per-point reconstruction loss and the point-wise squared error at each time step for two selected routes. Most test data points exhibit low losses, but a subset shows significantly

higher values. The normal route (blue) maintains consistently low loss values, whereas the anomalous route (red) exhibits sharp spikes in localized time intervals, indicating unexpected navigational and behavioral patterns.

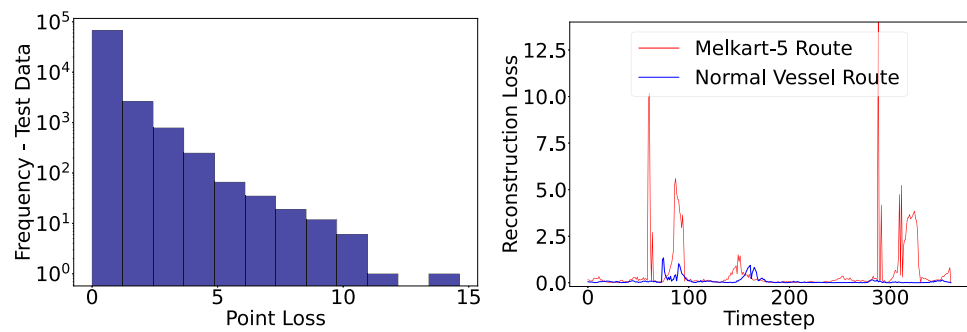
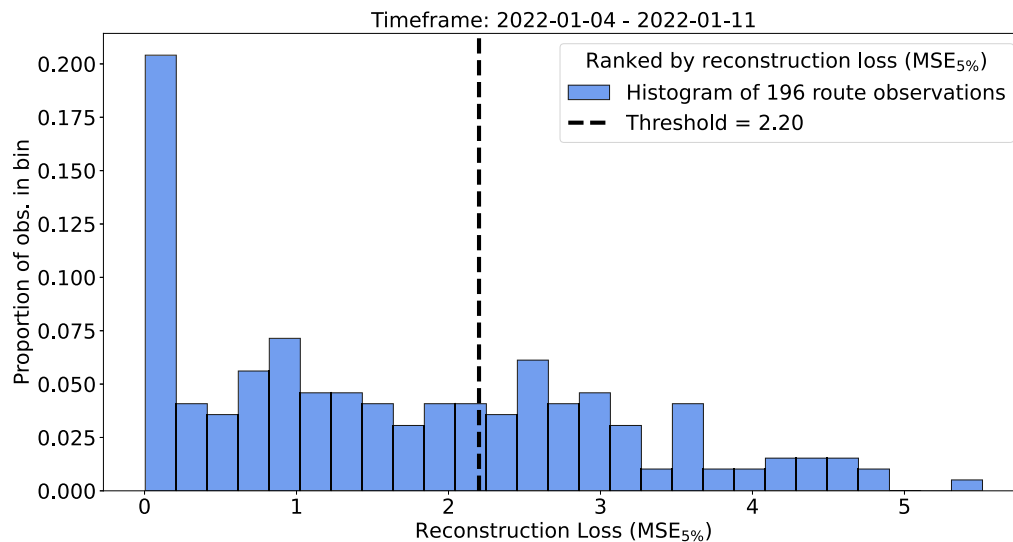


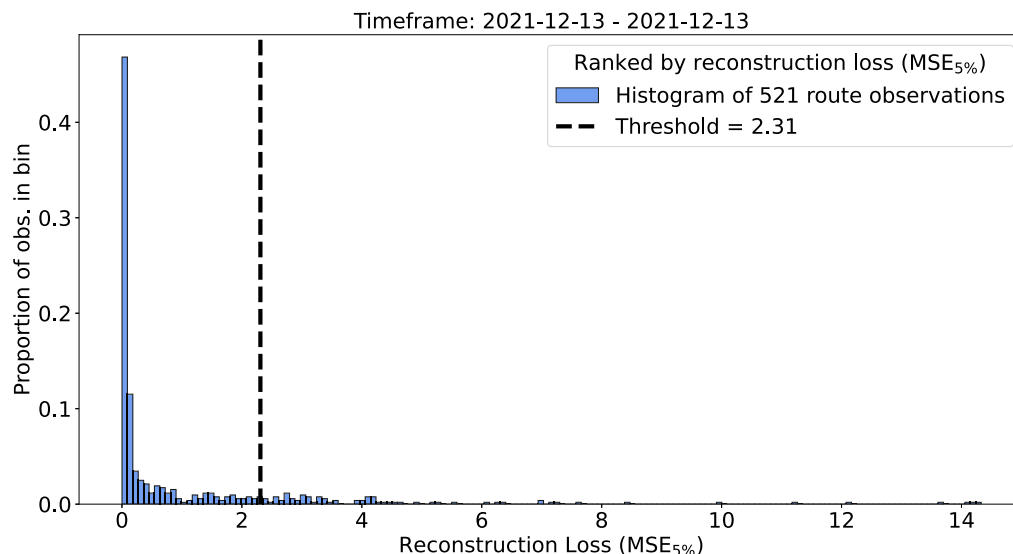
Fig. D.13. Left figure: Histogram of the point-wise reconstruction errors for all test trajectories in the Svalbard data. Right figure: Examples of the reconstruction error between the input trajectory \mathbf{x} and the reconstructed trajectory $\hat{\mathbf{x}}$ for a normal route (blue) and an abnormal route for MELKART-5 (red).

Appendix E. Reconstruction error distributions

The two regions exhibit markedly different error distributions. Svalbard (top figure) shows a more uniform distribution without a distinct outlier tail. Bornholm (bottom figure), however, has approximately 50 % of trajectories with $MSE_{5\%}$ values near zero, followed by a long tail of extreme anomaly values. These distributional differences explain why establishing a common threshold (vertical dashed line) across regions is challenging, as a single threshold would affect each distribution differently, directly impacting the model's generalizability Fig. E.14.



(a) Histogram of $MSE_{5\%}$ for Svalbard with an optimal threshold (τ) value of 2.40.



(b) Histogram of $MSE_{5\%}$ for Bornholm with an optimal threshold (τ) value of 2.31.

Fig. E.14. Histograms of reconstruction error for the Svalbard and Bornholm regions. The x-axis represents the $MSE_{5\%}$ for a given trajectory in the test data, while the y-axis shows the total proportion of $MSE_{5\%}$ per bin.

Appendix F. Baseline models

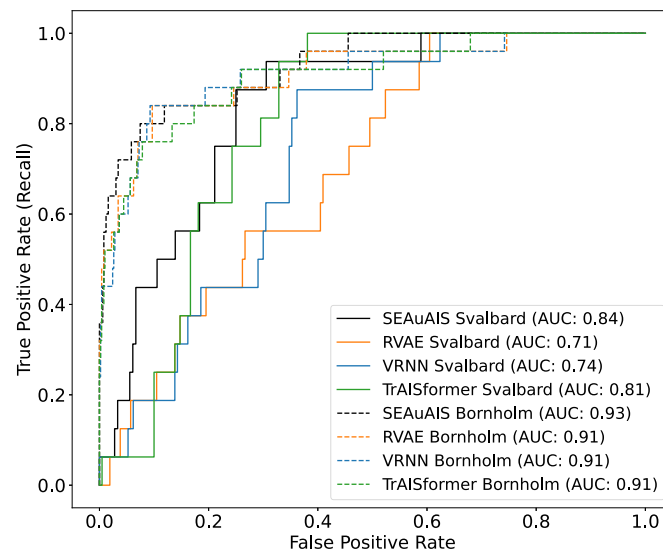


Fig. F.15. Comparison of ROC curves for SEAuAIS and baseline models (VRNN, RVAE, TrAISformer) on the Bornholm and Svalbard datasets. SEAuAIS results are shown in black (dashed for Bornholm, solid for Svalbard), while baseline models are color-coded. The legend indicates the model, region, and corresponding AUC score.

Fig. F.15 shows the ROC curves for AUCs obtained in Table 3.

Hyperparameters used for the three baseline models. For further details, see the code [repository](#).

Table F.7

Training times for each baseline model on the Svalbard and Bornholm datasets. All models were trained on the same system specifications as SEAuAIS (see Appendix C).

Model	Svalbard	Bornholm
VRNN	21 h 25 min	42 h 35 min
RVAE	3 h 26 min	8 h 12 min
TrAISformer	4 h 32 min	11 h 54 min

Table F.8

Model, dataset, and training hyperparameters for Bornholm and Svalbard. For VRNN and TrAISformer, the architecture (input/output dimensions, embedding sizes) is region-dependent due to binning. TrAISformer does not use a traditional encoder/decoder. See code for full details.

Parameter	RVAE		VRNN		TrAISformer	
	Bornholm	Svalbard	Bornholm	Svalbard	Bornholm	Svalbard
<i>Dataset & Preprocessing</i>						
Input Type	Continuous	Continuous	Four-hot (Discrete)	Four-hot (Discrete)	Four-hot (Discrete)	Four-hot (Discrete)
Lat Bins	N/A	N/A	150	300	150	300
Lon Bins	N/A	N/A	300	1000	300	1000
SOG Bins	N/A	N/A	40	40	40	40
COG Bins	N/A	N/A	72	72	72	72
Feature Dimension (Input)	5	5	562	1412	562	1412
<i>Model Architecture</i>						
Encoder/Decoder	GRU/GRU	GRU/GRU	LSTM/MLP	LSTM/MLP	Transformer blocks	Transformer blocks
Latent Dim	100	100	100	100	N/A	N/A
Recurrent Dim	100	100	100	100	N/A	N/A
Embedding Layers	N/A	N/A	N/A	N/A	[150,300,40,72]	[300,1000,40,72]
Output Head Dim	5	5	562	1412	562	1412
Transformer Layers	N/A	N/A	N/A	N/A	8	8
Attention Heads	N/A	N/A	N/A	N/A	8	8
MLP Inner Dim	N/A	N/A	N/A	N/A	3072	3072
Dropout	N/A	N/A	N/A	N/A	0.1	0.1
Blur Module	N/A	N/A	N/A	N/A	Yes	Yes
<i>Training Parameters</i>						
Optimizer	Adam	Adam	Adam	Adam	Adam	Adam
Learning Rate	0.001	0.001	0.001	0.001	0.001	0.001
Epochs	50	50	50	50	50	50
Batch Size	32	32	32	32	32	32
KL Weight	1	1	1	1	N/A	N/A

References

- AP News, 2023. Taiwan suspects Chinese ships cut islands' internet cables. <https://apnews.com/article/matsu-taiwan-internet-cables-cut-china-65f10f5f73a346fa788436366d7a7c700>.
- AP News, 2024. 3 Red Sea data cables cut as Houthis launch more attacks in the vital waterway. Section: World News. <https://apnews.com/article/red-sea-undersea-cables-yemen-houthi-rebels-attacks-b53051f61a41bd6b357860bbfb0b0860a>.
- Chandola, V., Banerjee, A., Kumar, V., 2009. Anomaly detection: a survey. ACM Comput. Surv. 41 (3), 1–58. <https://doi.org/10.1145/1541880.1541882>
- Chen, C., Li, O., Tao, D., Barnett, A., Rudin, C., Su, J.K., 2019. Deep learning for interpretable image recognition. Adv. Neural Inf. Process. Syst. 32, 801.
- Cuomo, S., Di Cola, V.S., Giampaolo, F., Rozza, G., Raissi, M., Piccialli, F., 2022. Scientific machine learning through physics-informed neural networks: where we are and what's next. J. Sci. Comput. 92 (3), 88. <https://doi.org/10.1007/s10915-022-01939-z>
- Flaaten, G., Eriksen, A.G., Elvevold, E.B., 2025. Russian trawlers passed over the Internet cable more than 30 times. Then it stopped working. <https://ground.news/article/russian-trawlers-passed-over-the-internet-cable-more-than-30-times-then-it-stopped-working>.
- Flaaten, G., Eriksen, A.G., Elvevold, E.B., 2022. Russisk tråler passerte over internettkabelen mer enn 30 ganger. Så sluttet den å virke. <https://e24.no/i/G3bM5V>.
- Gautam, S., Boubekki, A., Hansen, S., Salahuddin, S.A., Jenssen, R., Höhne, M. M.C., Kampffmeyer, M., 2022. ProtoVAE: A Trustworthy Self-Explainable Prototypical Variational Model. eprint: 2210.08151. <https://arxiv.org/abs/2210.08151>.
- Guo, S., Mou, J., Chen, L., Chen, P., 2021. An anomaly detection method for AIS trajectory based on kinematic interpolation. J. Mar. Sci. Eng. 9 (6), 609. Publisher: Multidisciplinary Digital Publishing Institute. <https://doi.org/10.3390/jmse9060609>
- International Maritime Organization (IMO), 2025. AIS transponders. <https://www.imo.org/en/OurWork/Safety/Pages/AIS.aspx>.
- Karageorgos, N., 2024. Anomaly Detection for Maritime Traffic, Anomali Detektion af Maritim Trafik. Master's thesis, DTU Department of Applied Mathematics and Computer Science.
- Karniadakis, G.E., Kevrekidis, I.G., Lu, L., Perdikaris, P., Wang, S., Yang, L., 2021. Physics-informed machine learning. Nat. Rev. Phys. 3 (6). Institution: Brown Univ., Providence, RI (United States) Publisher: Springer Nature. <https://doi.org/10.1038/s42254-021-00314-5>
- Kjærsgaard, R., Boubekki, A., Clemmensen, L., 2024. Pantypes: diverse representatives for self-explainable Models. In: Proceedings of the AAAI Conference on Artificial Intelligence. Vol. 38, pp. 13230–13237. Issue: 12.
- Kystdatahuset, 2024. AIS Positions within geometry and time API. Kystdatahuset API Documentation <https://kystdatahuset.no/ws/api/ais/positions/within-geom-time>.
- Maganaris, C., Protopapadakis, E., Doulamis, N., 2024. Outlier Detection in Maritime Environments Using AIS Data and Deep Recurrent Architectures. <https://doi.org/10.48550/arXiv.2406.09966>
- Marine Accident Investigation Branch, 2023. Report on the investigation of the collision between the general cargo vessel Scot Carrier and the split hopper barge Karin Høj resulting in the capsizing of the barge with two fatalities in the Bornholmsgat traffic separation scheme, Sweden on 13 December 2021. Accident Report 5/2023. Marine Accident Investigation Branch. <https://dmaib.dk/Media/638297625216175630/ScotCarrier-KarinHøj-ReportAndAnnex.pdf>.
- McInnes, L., Healy, J., Saul, N., Großberger, L., et al., 2018. UMAP: Uniform manifold approximation and projection. J. Open Source Softw. 3 (29), 861. <https://doi.org/10.21105/joss.00861>
- Murray, B., Perera, L.P., 2021. An AIS-based deep learning framework for regional ship behavior prediction. Reliab. Eng. Syst. Saf. 215, 107819.
- NATO, 2019. Strategic importance of, and dependence on, undersea cables. <https://ccdcoe.org/uploads/2019/11/Undersea-cables-Final-NOV-2019.pdf>.
- NATO, 2024. NATO holds first meeting of Critical Undersea Infrastructure Network. https://www.nato.int/cps/en/natohq/news_225582.htm.
- Nguyen, D., Fablet, R., 2021. Traisformer-a generative transformer for AIS trajectory prediction. ArXivabs:2109.03958.
- Nguyen, D., Fablet, R., 2024. Traisformer – a transformer network with sparse augmented data representation and cross entropy loss for AIS-based vessel trajectory prediction. IEEE Access 12, 21596–21609. <https://doi.org/10.1109/ACCESS.2024.3349957>
- Nguyen, D., Simonin, M., Hajduch, G., Vadaine, R., Tedeschi, C., Fablet, R., 2020. Detection of Abnormal Vessel Behaviours from AIS Data Using GeoTrackNet: From the Laboratory to the Ocean. <https://doi.org/10.48550/arXiv.2008.05443>
- Nguyen, D., Vadaine, R., Hajduch, G., Garello, R., Fablet, R., 2021. Geotracknet-a maritime anomaly detector using probabilistic neural network representation of AIS tracks and a contrario detection. IEEE Trans. Intell. Transp. Syst. 23 (6), 5655–5667.
- Olesen, K.V., 2023. Enhancing Situation Awareness of Maritime Surveillance Operators using Deep Learning based Abnormal Maritime Behaviour Detection. PhD Thesis. Technical University of Denmark.
- Olesen, K.V., Boubekki, A., Kampffmeyer, M.C., Jenssen, R., Christensen, A.N., Hørluck, S., Clemmensen, L.H., 2023a. A contextually supported abnormality detector for maritime trajectories. J. Mar. Sci. Eng. 11 (11), 2085. Publisher: MDPI.
- Olesen, K.V., Christensen, A.N., Clemmensen, L.H.K., 2023b. AIS Trajectories from Danish Waters for Abnormal Behavior Detection. https://data.dtu.dk/collections/AIS_Trajectories_from_Danish_Waters_for_Abnormal_Behavior_Detection/6287841/1. <https://doi.org/10.11583/DTU.C.6287841.V1>
- Pomrenke, E., 2023. Russian Trawler Suspected of Espionage. <https://www.ice-landreview.com/news/russian-trawler-suspected-of-espionage/>.
- Schia, N.N., Gjesvik, L., Rødningen, I., 2023. The subsea cable cut at Svalbard January 2022: What happened, what were the consequences, and how were they managed? <https://www.nupi.no/en/publications/cristin-pub/the-subsea-cable-cut-at-svalbard-january-2022-what-happened-what-were-the-consequences-and-how-were-they-managed>.
- TeleGeography, 2025. Submarine Cable FAQs. <https://www2.telegeography.com/submarine-cable-faqs-frequently-asked-questions>.

Wolsing, K., Roepert, L., Bauer, J., Wehrle, K., 2022. Anomaly detection in maritime AIS tracks: a review of recent approaches. *J. Mar. Sci. Eng.* 10 (1), 112. Number: 1 Publisher: Multidisciplinary Digital Publishing Institute. <https://doi.org/10.3390/jmse10010112>

Ziady, H., 2024. Red Sea cables have been damaged, disrupting internet traffic | CNN Business. <https://www.cnn.com/2024/03/04/business/red-sea-cables-cut-internet/index.html>.